Research Square

Preprints are preliminary reports that have not undergone peer review.
They should not be considered conclusive, used to inform clinical practice,
or referenced by the media as validated information.

Flow solver verification en route to virtual flight in realistic atmospheric environments

Moritz Spraul

moritz.spraul@dlr.de

Deutsches Zentrum für Luft- und Raumfahrt e. V. (DLR)

Anton Stephan

Deutsches Zentrum für Luft- und Raumfahrt e. V. (DLR)

Frank Holzäpfel

Deutsches Zentrum für Luft- und Raumfahrt e. V. (DLR)

Research Article

Keywords: Wake Vortex, LES, CODA, Overset

Posted Date: November 11th, 2026

DOI: https://doi.org/10.21203/rs.3.rs-11180317/v1

License: This work is licensed under a Creative Commons Attribution 4.0 International License.
Read Full License

Additional Declarations: No competing interests reported.

Flow solver verification en route to virtual flight in realistic atmospheric environments

Moritz Spraul[1*], Anton Stephan[1] and Frank Holzäpfel[1]

[1]Institute of Atmospheric Physics, German Aerospace Center, Münchener Straße 20, Oberpfaffenhofen, 82234, Germany.

*Corresponding author(s). E-mail(s): Moritz.Spraul@dlr.de;
Contributing authors: Anton.Stephan@dlr.de; Frank.Holzaepfel@dlr.de;

Abstract

The development of a simulation framework for virtual flight under realistic atmospheric conditions requires the accurate prediction of both aircraft aerodynamics and the evolution of coherent flow structures such as trailing vortices. In the present work, the CFD solver CODA is employed to investigate the formation, transfer, and downstream evolution of a wingtip vortex in an overset grid framework. A high-order discontinuous Galerkin discretization is applied to a rectangular NACA 0012 wing in a wind-tunnel configuration, with the vortex generator and surrounding flow domain represented by separate computational meshes coupled through overset interfaces. The vortex formation process is simulated using wall-modeled large-eddy simulation (WMLES). The study focuses on two primary objectives. First, the accurate prediction of the vortex-generation process through comparison with experimental and numerical reference data, and second the transfer and preservation of the resulting coherent vortex structure across computational domains. The results show that the high-order discontinuous Galerkin approach accurately captures the vortex roll-up process and preserves the turbulent vortex structure over extended downstream distances. Vortex meandering increases with downstream distance, while the dominant POD structures exhibit characteristic displacement patterns consistent with previous observations of trailing-vortex dynamics. Moreover, the overset coupling transfers the vortex between computational domains without significant loss of vortex strength or degradation of its characteristic structure. These results provide a basis for future virtual flight simulations involving interactions with atmospheric turbulence or wake vortices generated by other aircraft.

Keywords: Wake Vortex, LES, CODA, Overset

1 Introduction

The realization of virtual flight (VF) in realistic atmospheric environments requires an accurate CFD framework capable of capturing the aerodynamic interaction between an aircraft and its unsteady environment, thereby providing a relevant element of a digital twin for the flight through the atmosphere. Such simulations are relevant to several areas of aviation, including aircraft design, flight and airport operations and eventually certification. A comprehensive VF environment should capture both the aerodynamic response of the aircraft to atmospheric disturbances and the generation, evolution, and eventual decay of trailing vortices.

While current simulations accurately capture aerodynamic effects within uniform airflow, they often neglect the complex influence of atmospheric flow phenomena. Achieving a genuine virtual product requires coupling the aircraft model with its surrounding environment, bridging atmospheric physics and aircraft engineering through a unified and comprehensive approach. Such an environment enables the investigation of aircraft interactions with a wide range of atmospheric phenomena. Relevant influences are not limited to wake vortices but also include coherent disturbances such as gusts and waves, as well as convective and thunderstorm-induced turbulence. By representing these atmospheric processes realistically, VF can provide accurate estimates of the resulting aerodynamic forces and moments. This capability enables the virtual assessment of extreme events, fatigue loading, and predictive maintenance scenarios while reducing the dependence on costly flight experiments. Such simulations can further accelerate design optimization, support the development of advanced control and sensing systems, and potentially contribute to future certification processes through computational validation.

Coupling the atmospheric and aerodynamic domains represents a central component of VF. One promising approach is to employ separate computational grids for the different flow regimes. Such a decomposition allows numerical methods and turbulence models to be tailored to the respective flow physics. For example, different subgrid-scale models or numerical flux functions can be employed in each domain, potentially improving accuracy. The atmospheric model represents turbulence, gusts, and potentially wake vortices generated by other aircraft, while the aerodynamic model resolves their interaction with the flow around the aircraft geometry.

Accurately assessing the interaction between the wake of a leading aircraft and a trailing aircraft, for example, requires the generated vortices to evolve over sufficiently long periods to attain representative wake characteristics. Performing such simulations in an aircraft-centred reference frame would require prohibitively large computational domains to capture the downstream evolution of the wake. A more feasible approach is to employ a ground-fixed domain through which one or more aircraft move, allowing both wake evolution and subsequent aircraft-wake interactions to be simulated within the same computational environment [1, 2].

A ground-fixed reference frame offers several advantages for such simulations. First, environmental turbulence and coherent flow structures can be generated and evolved directly within the computational domain, avoiding the challenge to preserve them while introducing them through an inflow boundary condition. Second, high flow velocities relative to the stationary environment are largely confined to the vicinity of the

moving aircraft, potentially enabling an efficient incompressible treatment of large parts of the surrounding domain. Third, the complete temporal evolution of an aircraft wake, from its generation to its eventual decay, can be represented within the same computational domain. Finally, arbitrary aircraft trajectories can be considered, enabling the simulation of manoeuvrers such as take-offs, landings, and turns.

An advanced attempt to realize the VF concept was presented in [3]. Here all benefits of the aircraft-centered reference frame were demonstrated. However, the implementation remained too unpractical for a wider application due to the following reasons. First, the interface between the communicating domains in a finite volume setting contained multiple layers such that the memory requirements for complex geometries surpassed the resources. Second, the coupling of different flow solvers turned out to be too demanding for maintenance. In this study we aim to overcome these shortcomings while maintaining the capabilities of the VF concept.

Many engineering problems feature moving geometries, such as helicopters or wind turbines, which can be represented in CFD using methods like the arbitrary Lagrangian-Eulerian (ALE) technique [4]. However, ALE is generally limited to small displacements unless frequent re-meshing is employed. For large motions, sliding mesh or overset grid methods are more suitable. Sliding mesh approaches partition the computational domain into non-overlapping subregions that move relative to each other along their interfaces [5–7], but they struggle to accommodate the substantial translational and rotational movements typical of aircraft subjected to strong atmospheric disturbances. In contrast, overset grids enable fully independent motion of multiple overlapping meshes, with coupling achieved through interpolation of conserved variables across the overlapping regions [8–10]. This flexibility makes overset grids the preferred choice for VF.

Simulation of VF poses a demanding multiscale problem in computational fluid dynamics, involving a wide range of characteristic length and time scales. Relevant time scales extend from the rapid formation and roll-up of trailing vortices to their long-term evolution and eventual decay, including the development of instabilities such as the Crow instability [11]. At the same time, the spatial scales range from the thin boundary layers surrounding the aircraft to the considerably larger scales associated with atmospheric flow phenomena.

Numerical methods designed for high-order accuracy provide superior precision and efficiency in CFD and high-performance computing applications [12]. Many schemes, such as WENO [13], require wide stencils for solution reconstruction, which complicates overset-grid coupling. The discontinuous Galerkin (DG) method, by contrast, uses cell-local polynomials and exchanges information only with immediate neighbours via numerical fluxes from Riemann solvers [14, 15]. This compact stencil makes DG naturally well-suited for overset grids, as the coupling mechanism requires only minimal modification, limited to interpolating data at the artificial interface. DG also offers low numerical dissipation and robustness [16], making it ideal for simulating the complex, unsteady flow physics of aircraft-atmosphere interaction.

The simulations presented in this paper are performed using CODA, a next-generation CFD software jointly developed by ONERA, DLR, and Airbus. CODA is explicitly designed to leverage novel HPC architectures through multiple levels of

parallelization, including both shared and distributed memory [17]. It supports discretization of various equation systems using either finite volume or discontinuous Galerkin methods, combined with a wide selection of explicit and implicit time integration schemes. This versatility, along with the ability to utilize the DLR platform for multidisciplinary design analysis (FSDM) and its efficient parallelization, makes CODA well-suited for large-scale VF simulations.

The aim of this paper is the wall-modelled implicit large-eddy simulation (WMLES) of a wingtip vortex following the experiment of Chow et al. [18] using static overset grids. We focus on the influence of different spatial discretization schemes and resolutions on the trailing vortex and compare the results with experimental and computational references. Chow's test case has been extensively studied in recent years, particularly for the assessment of turbulence models, owing to the extensive experimental reference data available. Of particular interest in this regard is whether an implicit LES can accurately resolve the vortex roll-up process while simultaneously preserving the resulting vortex strength over multiple chord lengths downstream.

Recent numerical studies have addressed complex vortex-dominated flows over multi-swept and triple-delta wings, including vortex interactions, merging, and breakdown [19, 20]. Reinbold et al. [21] further investigated the vortical flow field of a delta-wing configuration using RANS simulations and overset grids. Kaufmann et al. [22] numerically investigated the formation and evolution of a blade-tip vortex on a finite wing and compared the results with experimental PIV data, demonstrating an increasing influence of numerical dissipation on the vortex characteristics with downstream distance. For Chow's configuration, several RANS studies have investigated the sensitivity of the near-field vortex to turbulence modelling and numerical resolution [23, 24]. Hybrid RANS-LES and other scale-resolving approaches have subsequently been employed to improve the prediction of the downstream vortex evolution and assess the influence of the numerical and modelling setup [25].

Large-eddy simulations have been conducted using a variety of numerical frameworks, including finite difference schemes on overset grids with Smagorinsky subgrid-scale modelling [26], as well as spectral/hp element methods combined with Spectral Vanishing Viscosity [27]. High-fidelity simulations approaching DNS resolution have further examined boundary-layer behaviour and its interaction with the vortex [28]. A key limitation of these studies is the systematic use of reduced Reynolds numbers to mitigate computational cost. The present work instead considers the experimental Reynolds number and employs a wall-modelled LES to relax near-wall resolution requirements. To the authors knowledge, this is the first application of a DGSEM based wall-modelled LES to Chows test case at the true Reynolds number.

The remainder of this paper is organized as follows. The spatial and temporal discretization schemes are presented in Section 2.1, followed by a description of the coupling interface in Section 2.2, while the evaluation of the Chow et al. test case can be found in Section 3. The paper concludes with Section 4 on recommendations for future development.

2 Numerical methods

We investigate the ability of numerical methods to capture the formation and persistence of a wingtip vortex. The scheme considered is the discontinuous Galerkin spectral element method (DGSEM), which is based on a subdivision of the computational domain into non-overlapping elements Ω_i, where a solution approximation using a polynomial representations is employed. The governing equations throughout this work are the compressible Navier–Stokes equations.

2.1 Discontinuous Galerkin spectral element method

The discontinuous Galerkin (DG) method employs a piecewise polynomial approximation of the solution within each element Ω_i

$$\boldsymbol{U}^{\Omega} \approx \sum_{p=1}^{N+1} \alpha_p(t)\varphi_p(\boldsymbol{x}), \tag{1}$$

where α denote the degrees of freedom and φ the basis functions. Multiplying the conservation equation with a test function, followed by integration over an element and insertion of the polynomial basis, yields the weak formulation

$$\int_{\Omega} \left(\boldsymbol{U}_t^{\Omega} + \nabla \cdot \boldsymbol{F}^S\right)\varphi dx = 0. \tag{2}$$

In the Galerkin formulation, the test functions coincide with the basis functions, for which one-dimensional Lagrange polynomials are employed. Each element contains $N+1$ degrees of freedom per spatial direction for a polynomial approximation of degree N. The integrals in the weak formulation are evaluated using numerical quadrature. High computational efficiency is achieved by collocating interpolation and integration nodes, thereby reducing the operation count per degree of freedom. The diffusive fluxes are discretized using the second method of Bassi and Rebay (BR2) [29]. For the convective fluxes, Roe's approximate Riemann solver [30] combined with the entropy fix of Harten and Hyman [31] is employed. Time integration is performed explicitly using a fifteen-stage, fourth-order low-storage Runge–Kutta scheme with an enlarged stability region [32]. The nodal distribution is based on Legendre–Gauss–Lobatto quadrature points. To improve robustness without introducing artificial viscosity, the split-form DGSEM formulation is employed. This formulation is based on the strong form of the conservation equations and provides entropy stability as well as kinetic-energy preservation [33].

2.2 Overset grids

In simulations involving multiple grids, the primary challenge lies in the coupling between adjacent domains. Depending on the spatial discretization, the coupling procedure differs slightly. In contrast to conventional Chimera approaches such as [3], the overset-grid methodology employed here does not require an overlap region between neighboring meshes. This approach reduces the memory requirements and enables

more complex aircraft geometries in the future. Instead, it is sufficient for the computational domains to share a common interface. This property allows larger portions of the background mesh to be removed, thereby reducing the total number of degrees of freedom. Overset, or artificial boundaries are treated as specialized boundary conditions. Their implementation is analogous to the communication procedure used at processor subdomain interfaces.

2.2.1 DGSEM coupling

Following the artificial-boundary method of Galbraith et al. [34], grid coupling is performed exclusively through numerical flux evaluations at artificial boundaries. Whereas fluxes at interior interfaces are computed solely from the left and right states of adjacent elements, the missing exterior state at an artificial boundary is provided by the overlapping donor grid (see Fig. 1). At each artificial interface, the $N+1$ flux evaluation points are distributed according to the selected nodal arrangement. Their physical coordinates, $\boldsymbol{x} = (x_1, x_2, x_3)$, are transferred to the donor grid, where the polynomial solution representation is used to evaluate the conserved variables and their gradients. These quantities are subsequently communicated back to the receiving grid. The transferred data then enables the artificial interfaces to be treated consistently with interior interfaces during numerical flux evaluation.

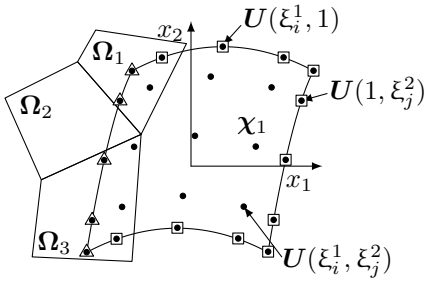


Fig. 1: Sketch of a DG cell χ_1 in physical space possessing one overset boundary overlapping with another grid. Volume solution points are denoted by dots, flux evaluation points by squares and artificial boundary points by triangles. The Legendre-Gauß-Lobatto point distribution is shown.

Although the identification of donor elements for each interface point introduces a non-negligible computational overhead, the method offers several important advantages. A primary benefit is the elimination of halo elements, which are typically required for solution reconstruction in high-order FV schemes. Furthermore, the number of flux evaluation points is reduced by a factor of $N+1$ compared to approaches based on reconstruction of the full volume solution. In FV methods, the stencil size generally increases with the formal order of accuracy, requiring additional halo cells at

overset interfaces. In contrast, the present DG approach maintains high-order accuracy using only the predefined interface flux points.

Direct pointwise evaluation of donor solutions at artificial boundaries introduces errors due to solution discontinuities and the loss of quadrature accuracy for non-smooth functions. To mitigate these effects, Farrell et al. [35] proposed a local Galerkin projection, while Crabill et al. [36] introduced a flux-reconstruction approach. Although these methods reduce overset interpolation errors, they also incur substantial additional computational cost. Galbraith et al. [34] and Spraul et al. [37] demonstrated that the associated errors decrease with increasing formal convergence order. Consequently, the simpler pointwise evaluation strategy is adopted in the present work, where it is shown to provide sufficient accuracy for the considered test cases.

3 Rectangular NACA 0012 wing

In this section, the ability of CODA to capture the formation and persistence of a wingtip vortex is assessed for different spatial discretizations. The primary challenge are the two different flow regimes present. First, the boundary layer undergoes roll-up into multiple vortical structures followed by their subsequent merging. Second, the resulting coherent vortex structure must be preserved over long propagation distances while minimizing numerical dissipation.

3.1 Geometry and grids

Only a limited number of test cases addressing wake-vortex formation provide detailed experimental reference data. One such configuration is the experiment conducted by Chow et al. [18]. The setup consists of a rectangular NACA 0012 wing with a chord length c and a rounded tip mounted inside a wind tunnel. The wing is attached to the tunnel wall and inclined at an angle of attack of ten degrees. Rotation is performed about the quarter-chord location, and the total wingspan is $0.75c$. The low-speed wind tunnel of the NASA Ames Research Center is represented by a rectangular computational domain with dimensions $10c \times 0.66c \times c$, as illustrated in Fig. 2. A Cartesian coordinate system is used with its origin located at the trailing edge of the wing.

To discretize the computational domain, two separate meshes are employed. The wing geometry and the channel section containing the wing root are resolved by the overlay grid, while the underlay grid represents the wind tunnel domain and includes sponge zones downstream of the inflow boundary and upstream of the outflow boundary. An overview of the mesh configuration is shown in Fig. 3. The underlay mesh consists of a Cartesian hexahedral discretization with hanging nodes. Local mesh refinement is applied in the vicinity of the wing and in the anticipated vortex path. The corresponding grid spacings are summarized in Tab. 1.

Generating a suitable mesh for the wing remains challenging, even for the comparatively simple geometry considered here, due to the requirement of purely hexahedral elements in the current DGSEM implementation. To address this issue, the commercial preprocessor ANSA was employed for generation of the overlay mesh. The resulting discretization corresponds to a structured C-grid around the NACA 0012 profile, extruded from the wing root and rotated about the wing tip.

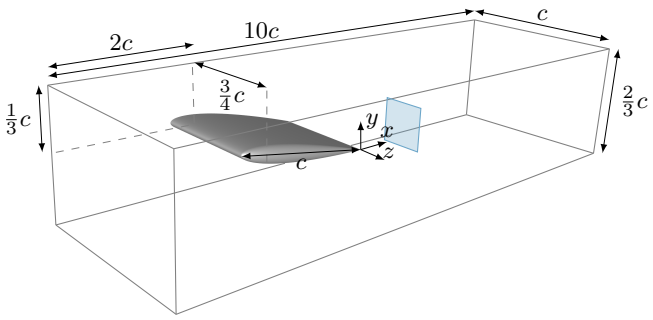


Fig. 2: Test section of the wind tunnel used by Chow et al. [18] as implemented in the simulation. One of the measuring planes used for flow analysis is shown in blue.

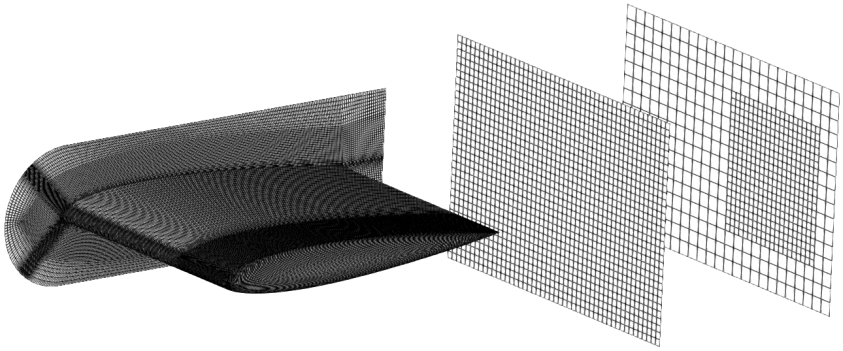


Fig. 3: Surface mesh of the wing and two slices in the yz-plane through the underlay.

3.2 Setup and initial conditions

The wing is exposed to a free-stream Mach number of $Ma_\infty = 0.15$. At the inflow and outflow boundaries, free-stream velocity and pressure conditions are prescribed. Consistent with previous numerical investigations of this configuration, inflow turbulence is not considered. Based on the reference flow quantities, the resulting Reynolds number with respect to the chord length is $Re_c = 4.6 \cdot 10^6$. In the experiments, the wing's boundary layer was tripped near the leading edge. For simplicity, the boundary layer in this setup is allowed to transition naturally from laminar to turbulent flow. Chow et al. [18] selected the wing dimensions to maximize the model size while avoiding viscous effects associated with the wind-tunnel boundary layers. Nevertheless, a pronounced inviscid blockage effect was observed. Lombard et al. [27] reported an effective increase in the angle of attack of approximately two degrees due to the limited cross-sectional

Table 1: Element sizes in different regions of the domain normalized by c.

	Boundary layer $[10^{-3}]$			Vortex nearfield $[10^{-3}]$			Vortex farfield $[10^{-3}]$		
	dx	dy	dz	dx	dy	dz	dx	dy	dz
DG-F	5.5	1.37	3.44	6.5	7.5	4.1	31.2	20.0	20.0
DG-M	11.0	2.74	6.88	12.7	15.6	7.7	31.2	20.0	20.0
DG-C	22.0	5.48	13.76	25.0	18.0	14.5	31.2	20.0	20.0

dimensions of the wind tunnel. In the present study, the wind-tunnel boundary layers are not resolved, and slip boundary conditions are imposed at the tunnel walls. This approach is consistent with the simulations of Uzun et al. [26] and Lombard et al. [27]. The simulations are initialized using a second-order accurate discretization and advanced until the temporal averages of the lift coefficient c_l and drag coefficient c_d, reach statistically stationary values. This state is reached after approximately nine convective time units (CTU). Subsequently, the polynomial degree of the DG ansatz is increased to the desired level. The simulation is then continued for an additional thirteen CTUs before collecting time-averaged statistics over a further four CTUs.

All quantities are evaluated on the measurement planes defined by Chow et al. which consist of point clouds in the yz-plane with a sampling resolution of approximately twice the polynomial order per computational element. The streamwise locations of the measurement planes relative to the trailing edge are listed in Table 2.

Table 2: Location of measuring planes normalized by c.

x/c	-0.394	-0.296	-0.197	-0.114	-0.005	0.005	0.125	0.246	0.452	0.678

3.3 Vortex core localization

Most quantities in the experiments of Chow et al. [18] are evaluated at the estimated centre of the vortex-core. Due to the steep gradients of all three velocity components in the vortex core, even small deviations of the detected core position can lead to significant discrepancies with respect to the experimental reference data. Several approaches for vortex-core identification have been proposed in the literature. Chow et al. [18] and Uzun et al. [26] defined the vortex centre as the location of minimum cross-flow velocity in the vicinity of the pressure minimum. In contrast, Lombard et al. [27] employed the local pressure minimum as the primary criterion, although a manual correction was applied. Stephan et al. [38] demonstrated that a combined criterion based on maximum vorticity and minimum pressure provides a robust approach for vortex tracking. Additional methods include identification based on extrema of helicity, the Q-criterion, or axial velocity. In the present study, the vortex-core position is

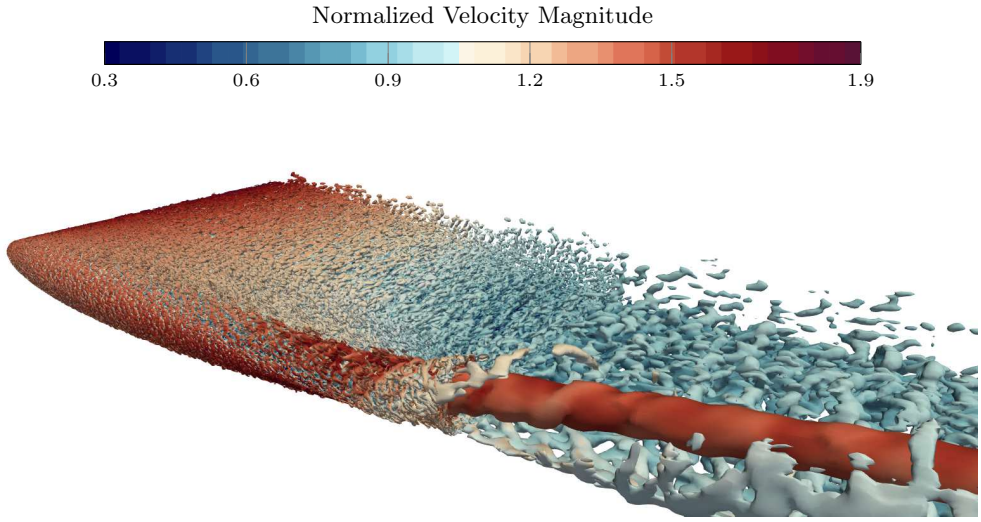


Fig. 4: Visualization of the instantaneous vortex structures around the NACA 0012 wing based on iso-surfaces of the Q-criterion.

determined similar to Chow et al. from the location of minimum cross flow velocity near the global pressure minimum, which was found to provide the most robust and consistent results. Determination of the vortex-core position is particularly challenging upstream of the trailing edge. In this region, multiple vortical structures are generated and subsequently merge, complicating the identification of a unique vortex centre.

Figure 4 shows an instantaneous visualization of the vortex roll-up process. Multiple vortical structures are generated in the vicinity of the wing tip and subsequently merge into the primary vortex. As a consequence, identification of a unique vortex core remains challenging in this region. Figure 5 shows a cross-sectional slice at $x/c = -0.296$ for several flow quantities together with vortex centres obtained using different identification criteria. Even in the time-averaged flow field, the vortex structure beneath the wing tip remains highly incoherent, making a consistent definition of the vortex core difficult.

Further downstream, the system of multiple vortices merges into an increasingly coherent structure. Figure 6 shows the axial velocity and pressure coefficient c_p at the vortex core as a function of the distance from the trailing edge. Downstream $x/c = 0.2$, the different core-identification criteria converge, indicating the formation of a more clearly defined dominant vortex core.

The vortex core exhibits a distinct meandering motion. No correction for the resulting contribution to the measured fluctuations is applied, as Chow et al. [18] considered this effect negligible and likewise did not correct their experimental data. A detailed analysis of the vortex meandering is provided in Section 3.4.3.

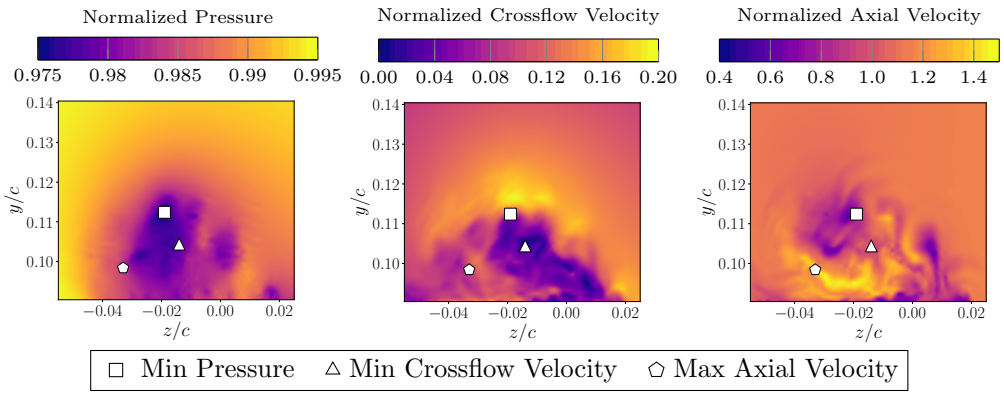


Fig. 5: Flow field in the yz-plane at $x/c = -0.296$ and the location of the vortex centre determined by different criteria.

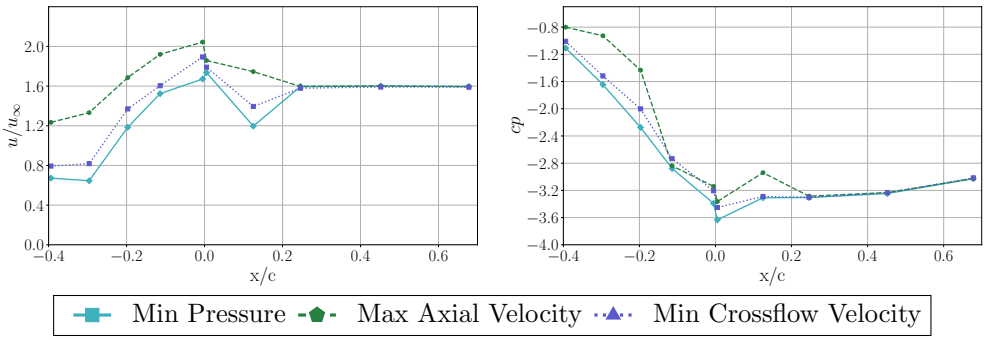


Fig. 6: Axial velocity (left) and c_p(right) over distance to trailing edge depending on the method used to define the vortex core.

3.4 Vortex evaluation

In this section, characteristic vortex quantities are evaluated and compared with the experimental results of Chow et al. [18] as well as previous computational studies. DGSEM discretization orders ranging from second to fourth order are considered by varying the polynomial degree.

3.4.1 Axial velocity and pressure coefficient

In Fig. 7 (left), the evolution of the axial velocity with respect to the distance from the trailing edge is shown. The discussion first focuses on the fourth-order DGSEM solution on the fine grid. In the first measurement plane at $x/c = -0.394$, a velocity deficit is observed in the vortex core. Further downstream, this deficit transitions into an axial velocity excess. The maximum is reached in the vicinity of the trailing edge,

where $u_{\mathrm{ax}} = 1.7\,u_\infty$, in good agreement with experimental data. With increasing distance from the trailing edge, the magnitude of the jet-like velocity excess gradually decreases, while a surplus is maintained. For the coarser grids, both results capture the initial increase in axial velocity but underpredict the experimental maximum. Nevertheless, the axial-velocity level at the final measurement plane is reproduced reasonably well. Convergence toward the experimental data in the lower-order DGSEM simulations is observed only downstream of the trailing edge, while no clear convergence is evident upstream. This behaviour is likely related to insufficient spatial resolution, as the highly unsteady vortex-formation process and the associated flow structures are particularly demanding to resolve accurately.

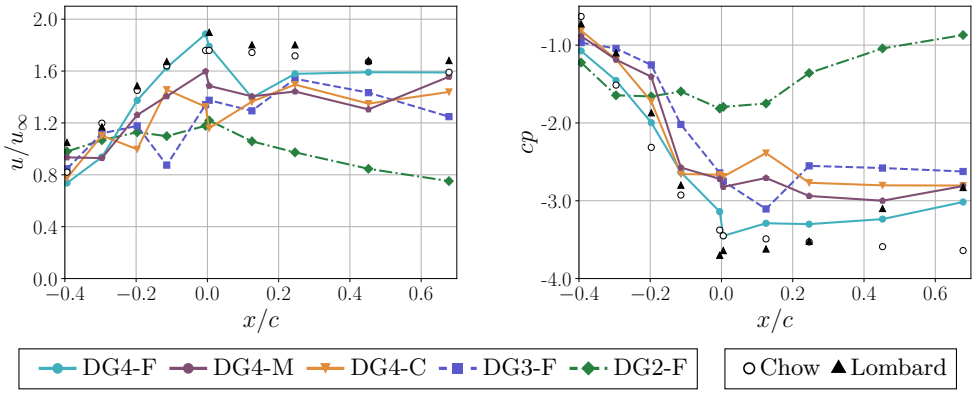


Fig. 7: Progression of axial velocity (left) and c_p (right) over distance to trailing edge. For comparison the results of Chow et al. [18] and the LES by Lombard et al. [27] are shown.

In Fig. 7 (right), the progression of the pressure coefficient

$$c_p = \frac{p - p_\infty}{\frac{1}{2}\,\rho u_\infty^2}, \tag{3}$$

is shown, where superscript ∞ denotes free-stream quantities. In the experiment, a pronounced reduction in static pressure is observed in the near wake. The minimum pressure occurs in the vicinity of the trailing edge, beyond which the pressure remains approximately constant in the downstream direction. This pressure minimum is associated with the vortex core formation and is consistent with the observed axial velocity increase. Rather than acting as a direct driving mechanism, the low-pressure region reflects the centrifugal balance within the swirling flow field and the associated radial pressure gradient sustaining the vortex structure.

Overall, the fourth-order DGSEM solution closely follows the experimental trend and captures the development of the pressure deficit. Further downstream, a gradual recovery of the pressure level is observed. DG4-M and DG4-C exhibit a similar evolution but under predict the magnitude of the pressure deficit. In the lower-order

DGSEM simulations, the results progressively converge toward both the higher-order solution and the experimental data.

3.4.2 Vortex position

In Fig. 8 (left), the vertical position of the vortex core relative to the trailing edge is shown. From the first measurement plane, the vortex core initially moves downward until it reaches a minimum position in the vicinity of the trailing edge. This trend is also captured by the numerical simulations. Further downstream, the vortex core exhibits an upward displacement.

The higher-order DGSEM solutions generally lie closer to the reference data, but no systematic convergence with increasing order is observed. Overall, the vertical evolution of the vortex trajectory is reasonably well reproduced by all schemes.

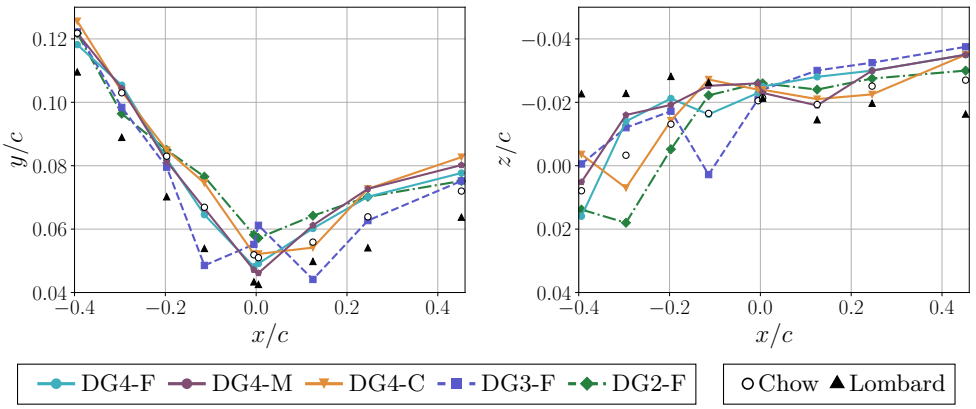


Fig. 8: Vertical and horizontal position of the vortex core in relation to the trailing edge. For comparison the result of Chow et al. [18] and LES by Lombard et al. [27] are shown.

Figure 8 (right) presents the axial evolution of the spanwise position of the vortex core. An inboard displacement is observed in the downstream direction. Similar to the trends in pressure and axial velocity, deviations in the lower-order solutions are more pronounced in the upstream region of the trailing edge, whereas better agreement with the reference data is obtained further downstream.

In the experimental data, a localized outboard displacement is observed around $x/c = 0.125$, which Chow et al. [18] attributed to the interaction and merging of a secondary vortex in this region. This secondary structure is induced by the primary vortex through its interaction with the boundary layer. A similar feature is also present in some of the fourth-order DGSEM results.

3.4.3 Vortex meandering

Vortex meandering refers to the low-frequency wandering of the vortex core about its mean axis and is a characteristic feature of trailing vortices observed in both experiments and numerical simulations [39–41]. Current evidence suggests that this motion is primarily the stochastic response of a dynamically receptive trailing vortex to disturbances associated with its formation and the surrounding flow [42]. Although the resulting displacement field resembles a helical vortex mode [43], this observation alone does not necessarily imply the presence of a self-excited instability.

Nevertheless the influence of meandering should be taken into account. Chow et al. assumed a sinusoidal lateral motion of the vortex centre at their last measurement plane at $x/c = 0.678$ with a meander amplitude of about 0.00010 c which was estimated to introduce an rms error of the crossflow velocity of 0.5% of the freestream velocity. In similar fashion the error for the Reynolds stresses was estimated and deemed negligible in the vicinity of the vortex generator ($x/c < 0.678$).

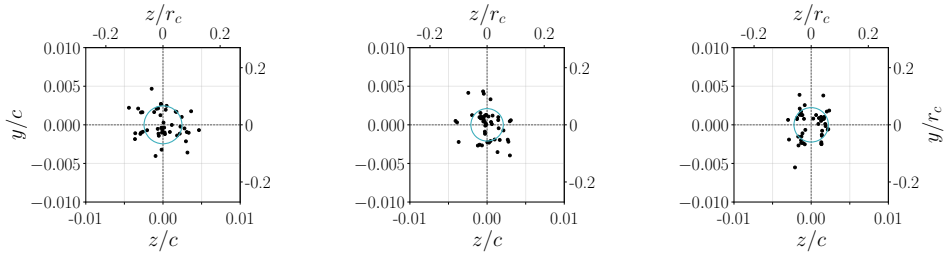


Fig. 9: Instantaneous core positions in the measuring planes at x/c = [1.0,2.0,3.0]. The origin is located at the vertical and horizontal coordinates of the mean vortex centre. The blue circles denote the average amplitude of the vortex wandering.

Figure 9 shows the instantaneous vortex-core positions at different locations downstream of the trailing edge. A distinct meandering motion is observed, with its amplitude initially decreasing slightly before increasing again further downstream. Devenport et al. [39] reported a linear increase in meandering amplitude between $x/c = 5$ and $x/c = 30$. The shorter downstream extent considered here, together with the proximity to the vortex-generating wing, may explain why a linear increase in meandering amplitude is not observed.

The Gaussian joint probability density function (JPDF) of the vortex-core positions, shown in Fig. 10, provides a compact representation of the spatial characteristics of the meandering motion. The elongated distributions indicate anisotropic vortex displacements, with the major axis defining a preferential direction of motion. An inclination of this axis relative to the coordinate directions further indicates a correlation between the lateral and vertical displacements. Both the amplitude and the preferential direction of the meandering vary with downstream distance. At $x/c = 3$ the mean radius of the meandering motion amounts already to 5.7% of the respective

vortex core radius as seen in Fig. 9. The vortex-core radius r_c is defined as the radial position at which the magnitude of the tangential velocity reaches its maximum.

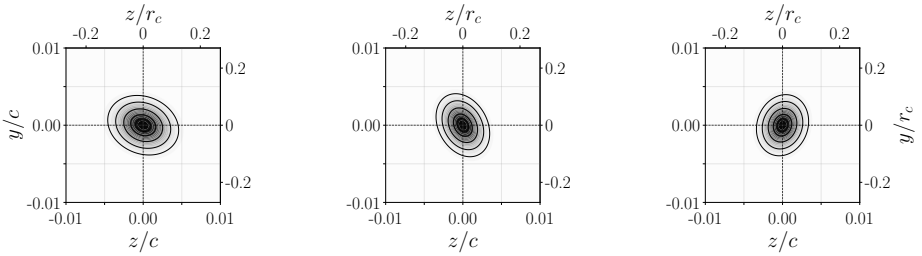


Fig. 10: Gaussian joint probability density distributions of the vortex core positions in the measuring planes at x/c = [1.0, 2.0, 3.0].

Azimuthally averaged normalised tangential-velocity profiles are presented in Fig. 11. The tangential velocity is evaluated in each measurement plane using a cylindrical coordinate system centred at the respective vortex-core positions determined at every instant of time used for the analysis. At each radial distance, the crossflow velocity components are interpolated along a circular contour parametrized by $y = r\cos\theta$ and $z = r\sin\theta$. The tangential velocity is then obtained by projecting the cross-plane velocity vector onto the circumferential direction according to

$$u_\theta = v\sin\theta - w\cos\theta. \tag{4}$$

The azimuthally averaged tangential-velocity profile is obtained as

$$\overline{u}_\theta(r) = \frac{1}{2\pi}\int_0^{2\pi} u_\theta(r,\theta)\mathrm{d}\theta. \tag{5}$$

With increasing distance from the trailing edge, both the magnitude of the tangential velocity and the core radius remain approximately constant. The variation of the velocity profiles associated with vortex meandering, represented by the shaded area, decreases slightly with downstream distance, consistent with the observed evolution of the meandering amplitude over the investigated range.

Following Hussain and Reynolds et al. [44], a triple decomposition of the flow field is performed to isolate the contribution associated with the wandering motion. The velocity vector at each sampling time t_i

$$\boldsymbol{u}(\boldsymbol{x},t_i) = \bar{\boldsymbol{u}}(\boldsymbol{x}) + \tilde{\boldsymbol{u}}(\boldsymbol{x},t_i) + \boldsymbol{u}^{'}(\boldsymbol{x},t_i) \tag{6}$$

is decomposed into the time-averaged component $\bar{\boldsymbol{u}}$, the coherent wandering component $\tilde{\boldsymbol{u}}$, and the turbulent fluctuation $\boldsymbol{u}^{'}$. Solving for the velocity fluctuations

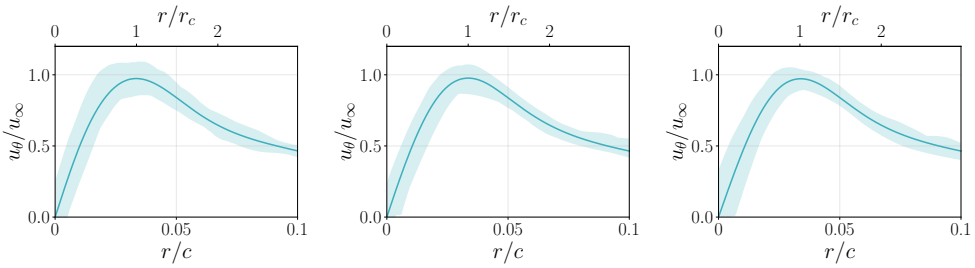


Fig. 11: Azimuthal average of normalised tangential velocity in measuring planes at x/c = [1.0,2.0,3.0]. The origin is located at the vertical and horizontal coordinates of the mean vortex centre.

associated with the meandering motion gives

$$\tilde{\boldsymbol{u}}(\boldsymbol{x}, t_i) = \Big[\boldsymbol{u}(\boldsymbol{x}, t_i) - \overline{\boldsymbol{u}}(\boldsymbol{x})\Big] - \Big[\hat{\boldsymbol{u}}(\boldsymbol{x}, t_i) - \overline{\hat{\boldsymbol{u}}}(\boldsymbol{x})\Big]. \tag{7}$$

The first term on the right-hand side is obtained directly from the instantaneous and time-averaged flow fields and contains contributions from both vortex wandering and turbulent fluctuations. The second term is introduced to separate the turbulent contribution from the wandering motion. For this purpose, the instantaneous snapshots in each measurement plane are shifted such that the instantaneous vortex core coincides with the corresponding mean vortex-core position. This transformation yields the vortex-centered flow field $\hat{\boldsymbol{u}}(\boldsymbol{x} - \boldsymbol{x}_c(t), t_i)$, in which the displacement associated with vortex meandering has been removed. The corresponding mean flow is then obtained by

$$\bar{\hat{\boldsymbol{u}}}(\boldsymbol{x}) = \frac{1}{M} \sum_{i=1}^{M} \hat{\boldsymbol{u}}(\boldsymbol{x} - \boldsymbol{x}_c(t_i), t_i) \tag{8}$$

Proper Orthogonal Decomposition (POD), following Sirovich et al. [45], is applied to identify the dominant spatial structures associated with the wandering motion.

Figure 12 shows the downstream evolution of the leading POD mode for each velocity component. Edstrand et al. [43] reported a pronounced interaction between the wake and the vortex in the stream wise velocity component at $x/c = 1.0$. A similar coupling is observed in the present results, although with a lower intensity. With increasing downstream distance, the dominant vortex structure becomes more decoupled from the wake and develops a characteristic helical pattern. The leading POD mode for the velocity in x direction exhibits a pronounced dipole-like structure in the vortex-core region, characteristic of a lateral displacement of the vortex. Its orientation approximately coincides with the major axis of the vortex-core JPDF (Fig. 10), suggesting that the mode represents the velocity-field signature of the preferential meandering motion.

For the transverse velocity components v and w, the largest modal amplitudes are concentrated around the vortex core, indicating a strong association with the

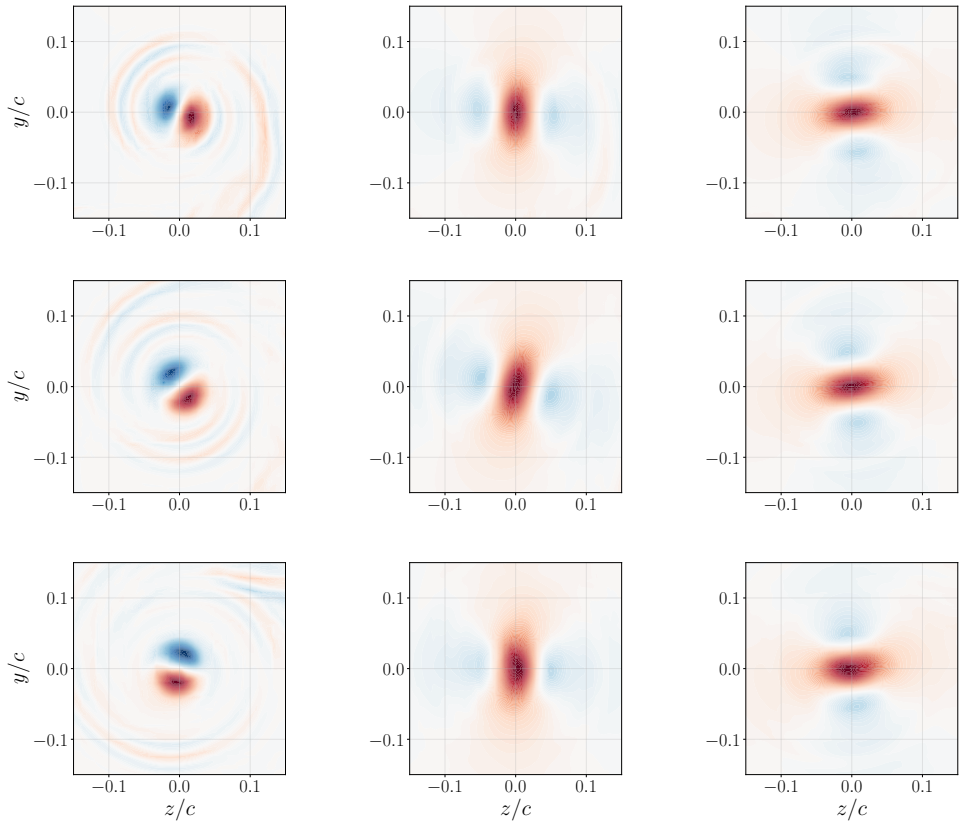


Fig. 12: Leading POD modes for meandering motion in x,y and z direction per column. Lines represent the downstream positions $x/c = [1.0,2.0,3.0]$.

meandering motion. The corresponding mode structures are oriented approximately perpendicular to each other, consistent with a radial displacement of the vortex core in the transverse plane. Overall, the leading modes exhibit spatial structures similar to those reported by Edstrand et al. [43], providing further evidence that the observed vortex meandering is consistent with the characteristic dynamics of trailing vortices as observed in a wind tunnel.

In Fig. 13 the downstream evolution of the modal kinetic energy is presented. The energy distribution provides a measure of the relative contribution of each POD mode to the vortex wandering. A pronounced concentration of energy in the first two modes indicates that the wandering motion is dominated by a small number of coherent structures rather than by broadband fluctuations. Higher-order modes contain progressively less energy and therefore contribute less to the overall wandering motion.

The total modal kinetic energy associated with the wandering component initially decreases and subsequently increases again over the investigated downstream

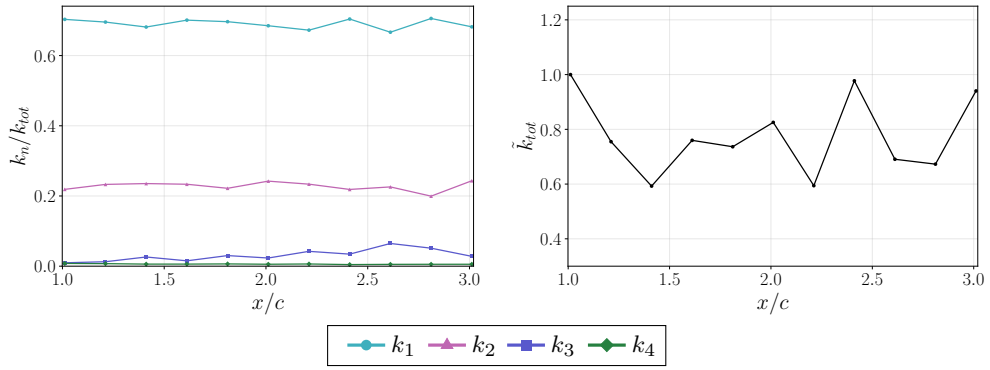


Fig. 13: Normalized kinetic energy k_n per POD modes n=[1,2,3,4] (left) and the total kinetic energy $\tilde{k}_{tot}$ normalized by the kinetic energy found in the plane at $x/c = 1.0$ (right).

range, without showing a clear overall amplification of the vortex meandering. This behaviour is consistent with the corresponding evolution of the instantaneous vortex-core displacement from its mean position over the same region.

3.4.4 Circulation

In the previous sections, the vortex formation process was investigated. The objective of the present section is to assess whether the resulting vortex can be sustained by the respective numerical schemes and to quantify the sensitivity of the vortex strength to variations in spatial resolution. To this end, the vortex circulation is considered as a primary measure of vortex intensity.

Experimental measurements of circulation were reported by Chow et al. [18] at a single measurement plane located at $x/c = 0.005$. Circulation was obtained by integrating the velocity field along a closed contour in the measurement plane. The same procedure is employed in the present study. Only limited information regarding the dimensions of the integration region in the y-z plane was provided. The experimental study merely states that the selected area was sufficiently large to encompass a substantial portion of the viscous wake. Chow et al. [18] reported a normalized circulation value of $\Gamma = 0.33$, where the normalization is defined as

$$\Gamma = \frac{\tilde{\Gamma}}{u_\infty c}. \tag{9}$$

Wake vortices are a direct consequence of lift generation on finite wings, and their strength is therefore closely related to the generated lift. Under the assumption of an elliptical circulation distribution, the circulation can be expressed in terms of the lift coefficient c_l, the aspect ratio Λ, and the wingspan b,

$$\Gamma = \frac{2 c_l u_\infty b}{\pi \Lambda}. \tag{10}$$

While an elliptical lift distribution represents an idealization that does not strictly reflect the loading of real wings [46], it nevertheless provides a useful first-order estimate of the expected vortex strength for the present simplified configuration.

Using the finest grid together with the fourth-order scheme results in a lift coefficient of $c_l = 0.739$. Based on the corresponding wing geometry, this corresponds to a normalised circulation of $\Gamma_{c_l} = 0.47$. The normalised circulation obtained by line integration of the velocity field over an area of $0.141c^2$, following the procedure of Chow et al., is $\Gamma_{\mathrm{LES}} = 0.427$. This lower value is consistent with the assumptions underlying the lift-based circulation estimate. The circulation estimated from the lift coefficient assumes an ideal elliptical spanwise loading, as predicted by classical lifting-line theory. The present configuration employs a rectangular wing with a realistic three-dimensional flow field, where viscous effects, finite aspect ratio, and tip-vortex formation produce a non-elliptical spanwise loading. Therefore, the lift-based estimate is expected to overpredict the circulation generated by the present wing.

Although both values deviate considerably from the experimental result, several factors must be taken into account. These include the assumption of an elliptical lift distribution, measurement uncertainty in the experimental data, and differences of the numerical and experimental setups discussed in Section 3.2.

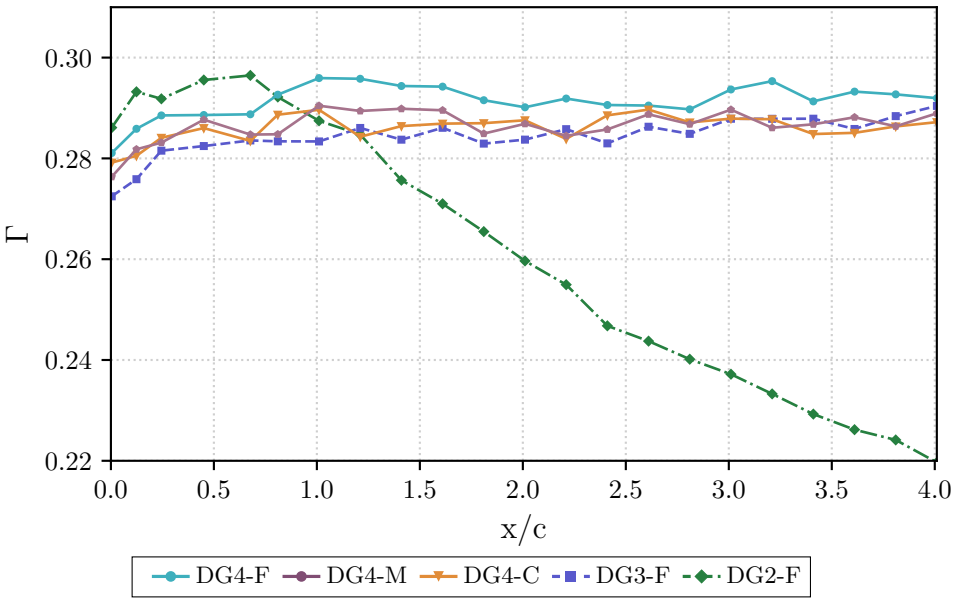


Fig. 14: Normalized circulation over distance to trailing edge.

Figure 14 shows the evolution of the normalised circulation as a function of distance from the trailing edge. The integration areas used for the computation of Γ are circles with radius $r = 0.1c$. They enclose multiple vortex core radii but do not cover the

majority of the wake. Consequently, the resulting circulation values are lower than the total circulation of the wake. Larger differences between the numerical schemes and spatial resolutions are observed up to approximately $x/c = 0.75$, primarily owing to differences in the vortex formation process. At this location, all schemes show good agreement in terms of circulation magnitude. Further downstream, DG-4-F predicts a slightly higher circulation than the other schemes, although the overall differences remain small.

The vortex is generated by the pressure difference between the suction and pressure sides of the wing, which is already captured at comparatively low spatial resolution. Its subsequent downstream evolution, however, is sensitive to numerical dissipation and spatial resolution. While the second-order DG scheme exhibits a rapid decay of circulation, the higher-resolution approaches preserve the vortex strength over several chord lengths downstream.

3.4.5 Reynolds stresses

Figure 15 shows the Reynolds stress R_{11} across the vortex at different downstream locations as reported by Chow et al. [47]. These velocity fluctuations in flow direction in the vortex core region are presumably caused by vortex core meandering, which responds highly sensitive to the characteristics of the surrounding turbulence [42]. Accordingly, the correct prediction of such non-stationary effects can be considered quite challenging. The core location was determined as before by the minimum of cross flow velocity. Experimental data are available from Chow et al. in the planes located at x/c = [-0.296,0.005,0.453].

At the measurement plane $x/c = -0.296$, where the vortex interacts with the wing boundary layer, the second-order scheme significantly over predicts the turbulence levels. The third-order DGSEM solution lies closer to the experimental reference in magnitude but exhibits a pronounced displacement of the vortex position. Only the fourth-order solution reproduces the experimental data reasonably well and captures the two distinct peaks observed in the measurements.

At the subsequent measurement plane (x/c = 0.005), the second-order DGSEM scheme appears overly dissipative and fails to reproduce the increased turbulence intensity accurately. The third-order solution, in contrast, substantially overpredicts the turbulence level, which may indicate oscillatory behaviour of the spatial approximation. The fourth-order scheme provides the best agreement, capturing both the position of the R_{11} peak and the overall turbulence level reasonably well.

Further downstream at $x/c = 0.453$, the Reynolds-stress magnitude is somewhat underestimated, which may be related to a delayed vortex-merging process. The experimental data exhibit a single distinct peak, while the numerical results retain a multi-peak structure. At $x/c = 2.011$, a single dominant peak is recovered for DG4-F, indicating that the vortex has developed into a more coherent structure further downstream. One possible explanation for the discrepancy at the upstream locations is the omission of a boundary-layer tripping mechanism in the simulations, which may alter the turbulence state entering the vortex-formation region.

Overall, preservation of the turbulent characteristics of the vortex core appears considerably more sensitive to numerical dissipation than the mean vortex quantities

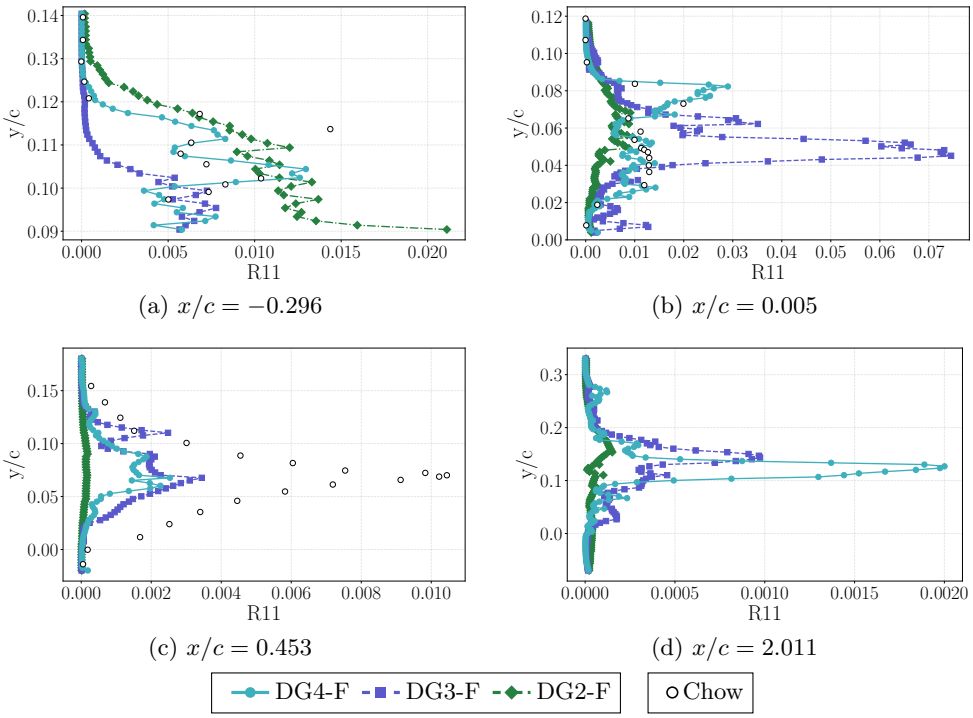


Fig. 15: Profiles of turbulent stresses across the vortex core a different yz - planes.

discussed previously. In particular, DG2-F does not sustain a pronounced vortex-core meandering motion, while the higher-order DGSEM schemes show a clear advantage in preserving the associated turbulent fluctuations over extended downstream distances.

3.4.6 Mean spanwise velocity

In Fig. 16, the mean spanwise velocity distribution through the vortex core is shown. In the measurement plane at $x/c = -0.296$, all numerical approaches capture the overall shape of the reference solution, with the fourth-order DGSEM scheme exhibiting the best agreement and accurately reproducing the vortex position.

Further downstream at $x/c = 0.005$, the second-order DGSEM solution is clearly unable to resolve the vortex flow adequately. Neither the velocity minima nor maxima are captured correctly, and discontinuities at element interfaces become visible. In the vicinity of the trailing edge, the higher-resolution schemes exhibit oscillatory behaviour near the velocity minima. Such oscillations are absent in both the experimental data and the second-order DGSEM results. Similar to the Reynolds stresses discussed previously, this behaviour may be associated with vortex meandering and the delayed merging of the secondary vortex structures.

In the final two measurement planes, the vortical structures have largely merged into a coherent vortex, and all numerical approaches except the second-order DGSEM scheme reproduce the reference data reasonably well.

Overall, the results indicate that accurate prediction of the mean vortex structure requires sufficient spatial resolution during the vortex roll-up process. While the higher-order DGSEM schemes preserve the characteristic velocity distribution throughout the downstream evolution, the lower-order approaches exhibit increased numerical dissipation and reduced accuracy in the near-wake region.

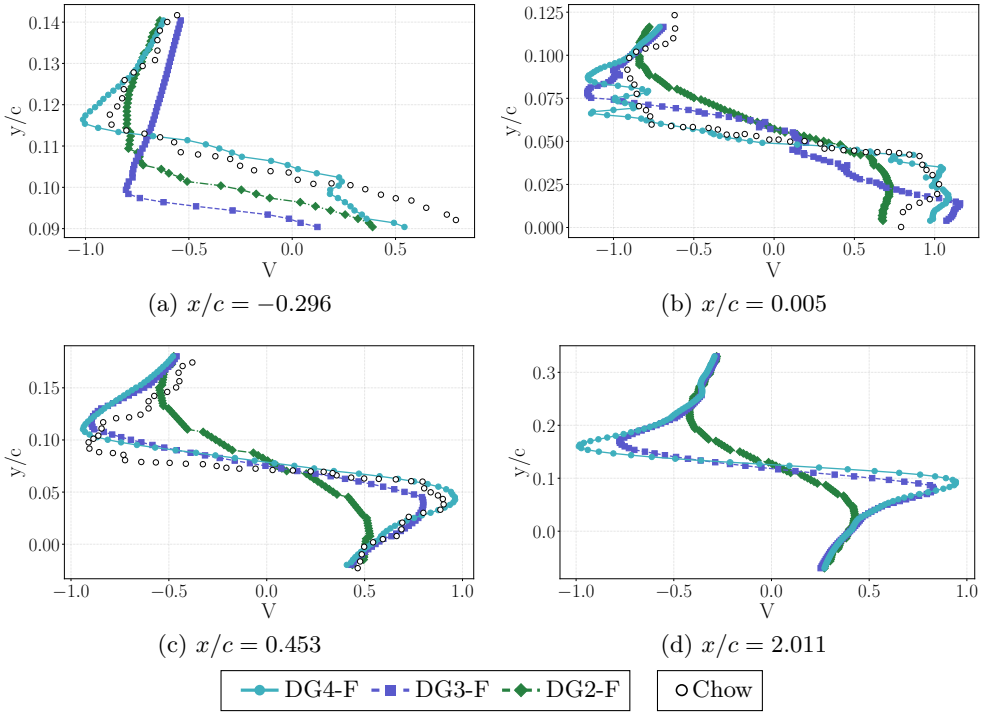


Fig. 16: Mean spanwise velocity across the vortex core a different yz - planes.

4 Conclusion

A setting for the realization of a virtual flight in a realistic environment with an aircraft-centred reference frame was proposed. For this purpose the CFD solver CODA with an overset-grid setup was utilized. To validate the approach, the formation and downstream evolution of a wingtip vortex were simulated as an implicit wall modelled LES using DGSEM with different polynomial degrees and computational grids. To the best of the authors knowledge, this study represents the first application of a DGSEM-based wall-modelled LES to Chows test case at the full experimental Reynolds number.

The fourth-order scheme on the fine grid shows very good agreement with the experimental reference in terms of axial velocity and pressure at the vortex core. Using lower polynomial orders and correspondingly fewer degrees of freedom still yields reasonably accurate predictions in the downstream region. However, the vortex roll-up and merging process upstream of the trailing edge is not captured with the same accuracy, where the fourth-order DGSEM approach exhibits a clear advantage.

It has been demonstrated that the implicit wall-modelled LES based on a high-order DGSEM scheme is capable of accurately capturing the turbulence levels within the vortex and sustaining its turbulent character far downstream of the trailing edge. The mean spanwise velocity distributions show overall good agreement with the reference data, with the fourth-order DGSEM solution again providing the closest match overall. However, the scheme tends to overpredict the velocity magnitudes in the downstream measurement planes.

Vortex strength, quantified in terms of circulation, is found to be only weakly dependent on spatial resolution during the formation phase. Since vortex generation is primarily driven by the pressure difference between the suction and pressure sides of the wing, the circulation can already be captured with comparatively low-order methods. In contrast, the long-term preservation of circulation and vortex coherence requires sufficient spatial resolution.

Overall, discretisations providing sufficient spatial resolution are able to reproduce the main features of the experimental flow field. In particular, the fourth-order DGSEM on the fine grid benefits from its high-order spatial accuracy and low numerical dissipation, enabling the vortex formation process to be accurately captured and its turbulent structure to be preserved over extended downstream distances. The results further demonstrate that, for the present wingtip-vortex flow, the DGSEM spatial operator can effectively act as an implicit subgrid-scale model, as good agreement with the reference data is obtained without introducing an explicit subgrid-scale model. Reducing the spatial resolution, either by mesh coarsening or by lowering the polynomial order, leads to a loss of accuracy in the prediction of the vortex roll-up process and its subsequent turbulent evolution. For applications where the primary objective is the prediction of the overall wake-vortex structure, this reduced level of accuracy may nevertheless be sufficient, particularly in view of the significantly lower computational cost. Preserving the turbulent character of the vortex over longer downstream distances, however, requires additional spatial resolution or a more elaborate turbulence-modelling approach.

The recent advances in HPC performance mostly stem from progress in compute performance, not memory bandwidth. This leads to memory-bound codes, such as finite volume methods, only speeding up by the gain in memory bandwidth, whereas (partly) compute-bound methods, such as the DGSEM, can also profit from the increased FLOP/s. This gets further aggravated by the move towards accelerator cards which have an even more unfavorable ratio of possible FLOP/s to memory bandwidth. With this in mind, a GPU port of CODA was started with the goal of enabling efficient WMLES simulations leveraging DGSEM.

A key limitation of the DGSEM approach is the requirement of purely hexahedral meshes, which typically requires significant meshing effort. While this is manageable

for the relatively simple configuration considered here, it becomes increasingly challenging for more complex aircraft configurations such as the Common Research Model. In such cases, finite volume methods, which are more flexible with respect to element types, may offer a more practical alternative, although they are limited to second-order accuracy in CODA.

The present study does not consider moving vortex generators. From a methodological point of view, grid motion can be handled within the overset-grid framework. The additional computational effort is primarily associated with repeated hole-cutting operations at each time step, as well as the re-initialization of solution values in cells that reappear from beneath the moving mesh. Consequently, the proposed methodology is not limited to stationary configurations but can also be extended to scenarios involving relative motion, such as formation flight, wake-vortex encounters or landing operations. The generated vortex can subsequently be transferred to a separate computational domain, where it may be used, for example, to simulate wake-vortex encounters while resolving the complex interaction between the incoming vortex and the encountering wing. Such simulations may reveal whether, under certain encounter conditions, phenomena such as flow separation can mitigate the resulting aircraft response.

By accurately reproducing the formation and downstream evolution of a realistic wingtip vortex, with key flow quantities in good agreement with experimental and numerical reference data, the applicability of CODA to virtual flight simulations has been demonstrated. In particular, the high-order DGSEM discretisation provides the spatial resolution required to capture and preserve the concentrated vortex structure over extended downstream distances. At the same time, CODA provides a versatile simulation framework in which the numerical discretisation and turbulence-modelling approach can be adapted to the physical problem under consideration, ranging from high-order DGSEM simulations as employed here to scale-resolving approaches such as detached-eddy simulation using a finite volume method. This versatility makes CODA particularly suitable for virtual flight applications involving a broad range of aerodynamic phenomena and levels of flow complexity.

Acknowledgments. The authors gratefully acknowledge Frank Spiering for providing efficient overset-grids and hole-cutting methods, and Miquel Herrera for his contributions to the implementation of hanging nodes for DGSEM and wall modelling. The authors further thank Axel Schwöppe for valuable discussions on gradient computation and Axel and Silvia Probst for productive discussions regarding scale-resolving simulations. The authors are also grateful to Stefan Görtz and Cord Rossow for their guidance and continued support throughout this work. The support of the entire Center for Computer Applications in AeroSpace Science and Engineering (CASE) is also greatly appreciated. CODA is the computational fluid dynamics (CFD) software being developed as part of a collaboration between the French Aerospace Lab ONERA, the German Aerospace Center (DLR), Airbus, and their European research partners. CODA is jointly owned by ONERA, DLR and Airbus. The authors gratefully acknowledge the scientific support and HPC resources provided by the German Aerospace Center (DLR). The HPC system CARA is partially funded by "Saxon State Ministry of Economic Affairs, Labour, Energy and Climate Action" and " Federal Ministry

of Research, Technology and Space". The HPC system CARO is partially funded by "Ministry of Science and Culture of Lower Saxony" and " Federal Ministry of Research, Technology and Space".

References

[1] Misaka, T., Holzäpfel, F., Gerz, T.: Large-eddy simulation of aircraft wake evolution from roll-up until vortex decay. AIAA Journal **53**(9), 2646–2670 (2015) https://doi.org/10.2514/1.J053671

[2] Stephan, A., Holzäpfel, F., Misaka, T.: Hybrid simulation of wake-vortex evolution during landing on flat terrain and with plate line. International Journal of Heat and Fluid Flow **49**, 18–27 (2014) https://doi.org/10.1016/j.ijheatfluidflow.2014.05.004 . 8th Symposium on Turbulence and Shear Flow Phenomena (TSFP8)

[3] Zholtovski, S., Stephan, A., Holzäpfel, F.: Towards virtual flight in realistic environments: A hybrid coupled simulation method. AIAA Journal **58**(3), 1266–1277 (2020) https://doi.org/10.2514/1.J058390

[4] Minoli, C.A.A., Kopriva, D.A.: Discontinuous galerkin spectral element approximations on moving meshes. Journal of Computational Physics **230**(5), 1876–1902 (2011) https://doi.org/10.1016/j.jcp.2010.11.038

[5] Weide, E., Kalitzin, G., Schluter, J., Alonso, J.: Unsteady Turbomachinery Computations Using Massively Parallel Platforms, p. 421 (2006). https://doi.org/10.2514/6.2006-421

[6] Duerrwaechter, J., Kurz, M., Kopper, P., Kempf, D., Munz, C.-D., Beck, A.: An efficient sliding mesh interface method for high-order discontinuous galerkin schemes (2020) https://doi.org/10.1016/j.compfluid.2020.104825

[7] McNaughton, J., Afgan, I., Apsley, D.D., Rolfo, S., Stallard, T., Stansby, P.K.: A simple sliding-mesh interface procedure and its application to the cfd simulation of a tidal-stream turbine. International Journal for Numerical Methods in Fluids **74**(4), 250–269 (2014) https://doi.org/10.1002/fld.3849

[8] Benek, J., Steger, J., Dougherty, F.C.: A flexible grid embedding technique with application to the Euler equations, (1983). https://doi.org/10.2514/6.1983-1944

[9] Galbraith, M.C., Benek, J.A., Orkwis, P.D., Turner, M.G.: A discontinuous galerkin scheme for chimera overset viscous meshes on curved geometries. Computers and Fluids **119**, 176–196 (2015) https://doi.org/10.1016/j.compfluid.2015.07.002

[10] Crabill, J., Witherden, F.D., Jameson, A.: A parallel direct cut algorithm for high-order overset methods with application to a spinning golf ball. Journal of Computational Physics **374**, 692–723 (2018) https://doi.org/10.1016/j.jcp.2018.

05.036

[11] Crow, S.C.: Stability theory for a pair of trailing vortices. AIAA Journal **8**(12), 2172–2179 (1970) https://doi.org/10.2514/3.6083

[12] Wang, Z.J., Fidkowski, K., Abgrall, R., Bassi, F., Caraeni, D., Cary, A., Deconinck, H., Hartmann, R., Hillewaert, K., Huynh, H.T., Kroll, N., May, G., Persson, P.-O., Leer, B., Visbal, M.: High-order cfd methods: current status and perspective. International Journal for Numerical Methods in Fluids **72**(8), 811–845 (2013) https://doi.org/10.1002/fld.3767

[13] Liu, X.-D., Osher, S., Chan, T.: Weighted essentially non-oscillatory schemes. Journal of Computational Physics **115**(1), 200–212 (1994) https://doi.org/10.1006/jcph.1994.1187

[14] Reed, W.H., Hill, T.R.: Triangular mesh methods for the neutron transport equation (1973)

[15] Cockburn, B., Shu, C.-W.: The runge-kutta discontinuous galerkin method for conservation laws v: Multidimensional systems. Journal of Computational Physics **141**(2), 199–224 (1998) https://doi.org/10.1006/jcph.1998.5892

[16] Gassner, G., Kopriva, D.A.: A comparison of the dispersion and dissipation errors of gauss and gauss-lobatto discontinuous galerkin spectral element methods. SIAM Journal on Scientific Computing **33**(5), 2560–2579 (2011) https://doi.org/10.1137/100807211

[17] Patel, H., Gerhold, T., Ashton, N.: Assessing the HPC Performance of CODA for the NASA Common Research Model. https://doi.org/10.2514/6.2024-3792

[18] Chow, J.S., Zilliac, G.G., Bradshaw, P.: Mean and turbulence measurements in the near field of a wingtip vortex. AIAA Journal **35**(10), 1561–1567 (1997) https://doi.org/10.2514/2.1

[19] Werner, M., Rein, M., Richter, K., Weiss, S.: Experimental and numerical analysis of the aerodynamics and vortex interactions on multi-swept delta wings. CEAS Aeronautical Journal **14**(4), 927–938 (2023) https://doi.org/10.1007/s13272-023-00678-7

[20] Di Fabbio, T., Tangermann, E., Klein, M.: Investigation of transonic aerodynamics on a triple-delta wing in side slip conditions. CEAS Aeronautical Journal **13**(2), 453–470 (2022) https://doi.org/10.1007/s13272-022-00571-9

[21] Reinbold, C., Sørensen, K., Breitsamter, C.: Aeroelastic simulations of a delta wing with a Chimera approach for deflected control surfaces. CEAS Aeronautical Journal **13**(1), 237–250 (2022) https://doi.org/10.1007/s13272-021-00561-3

[22] Kaufmann, K., Wolf, C.C., Merz, C.B., Gardner, A.D.: Correction to: Numerical investigation of blade-tip-vortex dynamics. CEAS Aeronautical Journal **9**(3), 387 (2018) https://doi.org/10.1007/s13272-018-0297-0

[23] Churchfield, M.J., Blaisdell, G.A.: Reynolds stress relaxation turbulence modeling applied to a wingtip vortex flow. AIAA Journal **51**, 2643–2655 (2013) https://doi.org/10.2514/1.J052265

[24] Cécora, R.-D., Radespiel, R., Eisfeld, B., Probst, A.: Differential reynolds-stress modeling for aeronautics. AIAA Journal **53**(3), 739–755 (2015) https://doi.org/10.2514/1.J053250

[25] Kolomenskiy, D., Paoli, R., Boussuge, J.-F.: Hybrid rans-les simulation of wingtip vortex dynamics. In: Proceedings of the ASME 2014 4th Joint US-European Fluids Engineering Division Summer Meeting Collocated with the ASME 2014 12th International Conference on Nanochannels, Microchannels, and Minichannels (2014). https://doi.org/10.13140/2.1.3635.0721

[26] Uzun, A., Hussaini, M.Y., Streett, C.L.: Large-eddy simulation of a wing tip vortex on overset grids. AIAA Journal **44**(6), 1229–1242 (2006) https://doi.org/10.2514/1.17999

[27] Lombard, J.-E.W., Moxey, D., Sherwin, S.J., Hoessler, J.F.A., Dhandapani, S., Taylor, M.J.: Implicit large-eddy simulation of a wingtip vortex. AIAA Journal **54**(2), 506–518 (2016) https://doi.org/10.2514/1.J054181

[28] Toosi, S., Peplinski, A., Schlatter, P., Vinuesa, R.: The impact of finite span and wing-tip vortices on a turbulent naca0012 wing. Journal of Fluid Mechanics **997** (2024) https://doi.org/10.1017/jfm.2024.667

[29] Bassi, F., Rebay, S.: A high-order accurate discontinuous finite element method for the numerical solution of the compressible navier-stokes equations. Journal of Computational Physics **131**, 267–279 (1997) https://doi.org/10.1006/jcph.1996.5572

[30] Roe, P.L.: Approximate riemann solvers, parameter vectors, and difference schemes. Journal of Computational Physics **43**(2), 357–372 (1981) https://doi.org/10.1016/0021-9991(81)90128-5

[31] Harten, A., Hyman, J.: Self-adjusting grid methods for one-dimensional hyperbolic conservation laws. Journal of Computational Physics **50**, 235–269 (1983) https://doi.org/10.1016/0021-9991(83)90066-9

[32] Niegemann, J., Diehl, R., Busch, K.: Efficient low-storage runge-kutta schemes with optimized stability regions. Journal of Computational Physics **231**(2), 364–372 (2012) https://doi.org/10.1016/j.jcp.2011.09.003

[33] Chandrashekar, P.: Kinetic energy preserving and entropy stable finite volume schemes for compressible euler and navier-stokes equations. Communications in Computational Physics **14**(5), 1252–1286 (2013) https://doi.org/10.4208/cicp.170712.010313a

[34] Galbraith, M.C., Benek, J.A., Orkwis, P.D., Turner, M.G.: A discontinuous galerkin chimera scheme. Computers and Fluids **98**, 27–53 (2014) https://doi.org/10.1016/j.compfluid.2014.03.014 . 12th USNCCM mini-symposium of High-Order Methods for Computational Fluid Dynamics

[35] Farrell, P.E., Maddison, J.R.: Conservative interpolation between volume meshes by local galerkin projection. Computer Methods in Applied Mechanics and Engineering **200**(1), 89–100 (2011) https://doi.org/10.1016/j.cma.2010.07.015

[36] Crabill, J.A., Sitaraman, J., Jameson, A.: A High-Order Overset Method on Moving and Deforming Grids, (2016). https://doi.org/10.2514/6.2016-3225

[37] Spraul, M., Stephan, A., Holzäpfel, F.: Towards a Simulation System for Virtual Flight - Dynamic High-Order Overset Grids Method. https://doi.org/10.2514/6.2024-1161

[38] Stephan, A., Holzäpfel, F., Misaka, T.: Aircraft wake-vortex decay in ground proximity-physical mechanisms and artificial enhancement. Journal of Aircraft **50**(4), 1250–1260 (2013) https://doi.org/10.2514/1.C032179

[39] Devenport, W.J., Rife, M.C., Liapis, S.I., Follin, G.J.: The structure and development of a wing-tip vortex. Journal of Fluid Mechanics **312**, 67–106 (1996) https://doi.org/10.1017/S0022112096001929

[40] Ranjan, R., Robinet, J.-C., Gaitonde, D.: Instability mechanisms in meandering streamwise vortex pairs of upswept afterbody wakes. European Journal of Mechanics - B/Fluids **96**, 90–104 (2022) https://doi.org/10.1016/j.euromechflu.2022.07.006

[41] Baba, S., Ben-Gida, H., Deng, G.C., Moreau, S., Stalnov, O., Lavoie, P.: Noise-generation mechanisms of a wing-tip vortex at moderate angle of attack. Journal of Fluid Mechanics **1026**, 18 (2026) https://doi.org/10.1017/jfm.2025.11001

[42] Boelle, T.: On the statistics of coherent vortices in incoherent environments. Physica A: Statistical Mechanics and its Applications (2023) https://doi.org/10.1016/j.physa.2023.128473

[43] Edstrand, A.M., Davis, T.B., Schmid, P.J., Taira, K., Cattafesta, L.N.: On the mechanism of trailing vortex wandering. Journal of Fluid Mechanics **801**, 1 (2016) https://doi.org/10.1017/jfm.2016.440

[44] Hussain, A.K.M.F., Reynolds, W.C.: The mechanics of an organized wave in

turbulent shear flow. Journal of Fluid Mechanics **41**(2), 241–258 (1970) https://doi.org/10.1017/S0022112070000605

[45] Sirovich, L.: Turbulence and the dynamics of coherent structures. i. coherent structures. Quarterly of Applied Mathematics **45**, 561–571 (1987) https://doi.org/10.1090/qam/910462

[46] Breitsamter, C.: Nachlaufwirbelsystem Großer Transportflugzeuge. Habilitationsschrift, Technische Universität München. Herbert Utz Verlag, München (2007)

[47] Chow, J.S., Zilliac, G.G., Bradshaw, P.: Measurements in the near-field of a turbulent wingtip vortex. In: 31st Aerospace Sciences Meeting. American Institute of Aeronautics and Astronautics, Reno, Nevada (1993)